LAWRENCE
LIVERMORE
NATIONAL
LABORATORY

UCRL-TR-200644

XPS Studies of $Yb_{14}MnSb_{11}$ and $Yb_{14}ZnSb_{11}$

A.P. Holm, T.C. Ozawa, S.M. Kauzlarich,
S.A. Morton, G.D. Waddill, W.E. Pickett, J.G. Tobin

October 2, 2003

This work was performed under the auspices of the U.S. Department of Energy by the University of California, Lawrence Livermore National Laboratory under Contract W-7405-Eng-48.

XPS Studies of $Yb_{14}MnSb_{11}$ and $Yb_{14}ZnSb_{11}$

Aaron P. Holm,[1] Tadashi C. Ozawa,[1] Susan M. Kauzlarich,[1*] Simon A. Morton,[2]

G. Dan Waddill,[2] Warren E. Pickett,[3] and James G. Tobin[4]

smkauzlarich@ucdavis.edu

[1]*Department of Chemistry, University of California, One Shields Ave., Davis, CA 95616*

[2]*Department of Physics, University of Missouri-Rolla, Rolla, MO 65401-0249*

[3]*Department of Physics, University of California, One Shields Ave., Davis, CA 95616*

[4]*Lawrence Livermore National Laboratory, Livermore, CA 94550*

Measurements of core and valence electronic states of single crystals of the rare earth transition metal Zintl phases $Yb_{14}MnSb_{11}$ and $Yb_{14}ZnSb_{11}$ were performed using the X-ray photoelectron spectroscopy station of Beamline 7 at the Advanced Light Source. Sample surfaces of $Yb_{14}MnSb_{11}$ and $Yb_{14}ZnSb_{11}$ were measured as received, after Ar^+ ion bombardment, and after cleaving *in situ*. Detailed analysis of the clean Mn and Zn analog sample surfaces reveal a significant contribution of both Yb^{3+} and Yb^{2+} 4*f* states in the valence band region for the Zn analog and no contribution of Yb^{3+} states to the valence band for the Mn analog. This result is predicted for the Zn analog by Zintl counting rules, and single crystal X-ray diffraction studies presented here also support the mixed valency of Yb for $Yb_{14}ZnSb_{11}$. Further detailed analysis of the core and valence band structure of both $Yb_{14}MnSb_{11}$ and $Yb_{14}ZnSb_{11}$ will be presented.

Introduction.

The family of transition metal compounds with the $Ca_{14}AlSb_{11}$ structure type[1] has shown a wide variety of unique electronic and magnetic properties.[2,3] In particular, the series $A_{14}MnPn_{11}$, show properties ranging from paramagnetic insulators to ferromagnetic metals, depending on the identity of A (alkaline earth or rare earth atom) and Pn (pnictogen atom). This class of compounds consists of an isolated magnetic cluster that can magnetically couple over large interionic distances (~1 nm). The magnetic exchange interaction has been attributed to a Ruderman-Kittel-Kasuya-Yosida (RKKY) interaction between localized moments via conduction electrons.[3] This structure type ($A_{14}MPn_{11}$) has been prepared to date with most 2+ cations such as A = Ca, Sr, Ba, Eu, and Yb, with M = Mn, Al, Ga, In, Nb, and Zn, and with Pn = P, As, Sb, and Bi.[1-26] One formula unit is composed of 14 A^{2+} cations, one MPn_4^{9-} tetrahedron, one Pn_3^{7-} unit, and 4 Pn^{3-} isolated anions. The structure has been interpreted according to the Zintl concept, which invokes charge balance between (usually) closed shell structural units such as complexes or extended covalent structures and ions. In this simple model, the Mn is 3+, similar to group 13 metals that also crystallize in this structure type. Both structure and magnetism measurements have been used to support this assignment.[3]

A recent report of X-ray magnetic circular dichroism (XMCD) measurements of the compound $Yb_{14}MnSb_{11}$ has produced new information on the source of the magnetic moment in this system, and has increased our understanding of the magnetic interactions in this structure type.[27] The element specific measurements reveal a large dichroism in the L_{23} absorption edge of Mn that is most consistent with Mn in a 2+ (d^5) configuration. In addition to the large Mn dichroism, a small dichroism is observed in the M_{45}

absorption edge of Sb. This absorption signal is antialigned to the Mn absorption, and indicates a small magnetic moment lies on Sb that is antialigned to the Mn moment. These results seem to be inconsistent with the value of ~4 μ_B/ formula unit previously reported from bulk magnetization measurements of the compounds that make up the $A_{14}MnPn_{11}$ structure type,[2,3,6-12,14,17-21,23-26,28] but a recent theoretical study of the bonding, moment formation and magnetic interactions of the related $Ca_{14}MnBi_{11}$ and $Ba_{14}MnBi_{11}$ systems suggests a new model to account for the discrepancy between electron counting and the experimental data.[29] This study indicates that these phases are nearly half-metallic, and that Mn is present in this structure as Mn^{2+}. It also predicts the presence of a polarized hole localized on the $MnPn_4$ tetrahedron lying parallel to the Mn moment, and resulting in a net $MnPn_4$ moment that is considerably reduced from the ionic Mn^{2+} value. The experimental results are consistent with this theoretical model.

Another report of thermodynamic, transport, and X-ray diffraction measurements of the related Zintl phase, $Yb_{14}ZnSb_{11}$, has also reported interesting new information related to the Yb analogs of this structure type.[30] This study compares data collected on the Mn, Al, and Zn analogues of this series. The unit cell volume reported from single crystal X-ray diffraction measurements of each of these compounds shows a steady change in volume, with the Zn analogue having the smallest unit cell volume. The magnetic susceptibility data are reported for $Yb_{14}ZnSb_{11}$, and show complex magnetic behavior with an effective moment of 3.8 ± 0.1 μ_B/ formula unit, and an average Weiss temperature of -273 ± 10 K. The electrical resistivity data reported for $Yb_{14}ZnSb_{11}$ demonstrate similar behavior to that for $Yb_{14}MnSb_{11}$, but more metallic behavior is demonstrated by the Zn analog in addition to a much broader drop in resistivity at ~ 85 K

in comparison to the sharp drop at 52 K by the Mn analog. The data reported for the Zn analog is explained in terms of an intermediate valence scenario for Yb. The combination of a metallic covalency and a contraction in the unit cell volume both support the presence of an intermediate valence, but are not conclusive evidence. A comparative study of these Zintl compounds by X-ray photoelectron spectroscopy should help shed new light on the question of whether an intermediate valence in Yb is present in the Zn analog, and is responsible for the bulk properties reported.

In this paper, we present X-ray photoelectron spectroscopy (XPS) characterization of the core and valence electronic states of $Yb_{14}MSb_{11}$ (M = Mn, Zn), and in addition, a more detailed crystal structure is presented for $Yb_{14}ZnSn_{11}$.

Experimental

Single crystal samples of both $Yb_{14}MnSb_{11}$ and $Yb_{14}ZnSb_{11}$ were grown by a high temperature molten metal flux synthesis as described elsewhere.[12,30,31] Single crystal X-ray diffraction data for $Yb_{14}ZnSb_{11}$ were acquired using a SMART 1000 Bruker AXS CCD diffractometer equipped with a CRYO COOLER low temperature apparatus (CRYO INDUSTRIES of America, Inc.). A dark grey crystal (1.5 mm x 1.4 mm x 1.6 mm) of $Yb_{14}ZnSb_{11}$ was cut into a smaller piece (0.03 mm x 0.178 mm x 0.142 mm), and it was mounted in the cold nitrogen gas stream (90 K) of the diffractometer. X-rays were generated at 50kV and 40mA using a Mo target and graphite monochromator. A total of 27196 reflections were collected for the full sphere using a 0.3° □-scan with a 30 seconds exposure. Previously published crystallographic data of the Mn analog, $Yb_{14}MnSb_{11}$,[7]

was used as a starting model for the refinement. This structure was refined utilizing the SHELXTL-97 software package[32] using 2493 unique reflections and 63 parameters.

Selected samples for the XPS measurements of both $Yb_{14}MnSb_{11}$ and $Yb_{14}ZnSb_{11}$ were characterized by comparing lattice parameters determined by single crystal X-ray diffraction to previously published results (references 7, 12 and 45), and also by magnetic susceptibility measurements. XPS measurements were performed in the UltraESCA endstation of Beamline 7.0.1. Samples were mounted on Mo pucks in air, and introduced to the preparation chamber (base pressure 2 _ 10^{-10} Torr). Initial attempts to clean the sample surfaces by Ar^+ sputtering over varying time periods (2-180 minutes) provided significant improvement from the "as-received" samples, but the best results for sample surface preparation were obtained by cleaving the crystal samples in the preparation chamber using a single blade cleaving tool, and then transferring them to the analysis chamber (1_ 10^{-10} Torr). Photoemission spectra were collected at T = 93 K and various photon energies ($h\square$) between 80 and 200 eV for the valence band scans, and 600 -1250 eV for the wide surveys and core state surveys. The binding energy of the photoemission structures was calibrated by the Fermi edge of a gold foil mounted next to the samples on the Mo pucks and Ar^+ sputtered immediately prior to cleaving.

Results and Discussion.

The refined crystal structure data for $Yb_{14}ZnSb_{11}$ is summarized in Tables 1~3. $Yb_{14}ZnSb_{11}$ crystallizes in the tetragonal space group $I4_1/acd$ (Z = 8). The structure of $Yb_{14}ZnSb_{11}$ is isostructural to the Mn analog, $Yb_{14}MnSb_{11}$, which consists of: 14 Yb^{2+} + $[MnSb_4]^{9-}$ (tetrahedron) + $[Sb_3]^{7-}$ (linear chain) + 4 $[Sb]^{3-}$.[7,12] The lattice parameters for

$Yb_{14}ZnSb_{11}$ are $a = b = 16.562(3)$ Å and $c = 21.859(2)$ Å at 90 K. The lattice parameters a and b are larger in the Zn analog than in the Mn analog (16.591(1) Å), whereas the lattice parameter c is smaller in the Zn analog than in the Mn analog (21.919(3) Å). The refinement of the site occupancy factor indicated the full occupancies (within the range of their standard deviations) in all sites except the Zn site. Thus, the final refinement was performed with the fixed and full occupancies in all Yb and Sb sites and variable Zn occupancy setting. This refinement shows the Zn occupancy of 0.976(11). The nearest Zn···Zn distance is 9.9216(13) which is slightly smaller than the Mn···Mn distance (9.9420(6)) in the Mn analog.

A comparison of scans of the Sb3d/O1s region (520-540 eV) of the "as-received" samples and those prepared under varying conditions is presented in Figure 1. No appreciable oxide contamination is present after cleaving of the crystal, but during scans aimed at maximizing the Mn 2*p* cross section, a slight contamination was observed when scanned at $h\nu = 900$ eV. In addition, a check for Sn contamination was also performed due to the growth conditions of the samples. Scans of the "as-received" samples show slight Sn contamination, but upon cleaving, all indications of Sn are removed as seen in the inset of Figure 2.

Figure 2 shows the wide survey photoemission spectrum of $Yb_{14}MnSb_{11}$ measured at $h\nu = 1250$ eV. The core level states for Yb, Mn and Sb are present and well resolved near the corresponding positions for the elements in their natural forms.[33] The Sb 3*s*, $3p_{1/2}$, $3p_{3/2}$, $3d_{3/2}$, $3d_{5/2}$, and 4*s* core levels are observed at binding energies of 952.0, 813.0, 772.0, 543.0, 534.0, and 158.0 eV respectively, and are within ~1 eV of the tabulated peak positions for the elemental form. The peak separations of the spin-orbit

split partners correspond to the tabulated differences to within ~1 eV difference. The states of Sb $4p_{1/2}$ and $4p_{3/2}$ core levels are not resolved, but peak intensity at 108.0 eV is present corresponding to Sb $4p$. The Yb $4s$, $4p_{1/2}$, $4p_{3/2}$, $4d_{3/2}$, and $4d_{5/2}$ core levels are present at binding energies of 486.0, 395.0, 345.0, 197.0, and 188.0 eV respectively. As with the Sb positions, the Yb peak positions are all within ~7 eV of the tabulated peak positions for the elemental form, and spin-orbit split peak differences are all within 1 eV of tabulated differences.

Figure 3 shows the valence band scan of $Yb_{14}MnSb_{11}$ measured at $h\nu$ = 120 eV. The general spectral shape of the complete region studied remained consistent over the complete photon energy range studied ($h\nu$ = 80-200 eV). The core level, spin-orbit split Sb $4d_{3/2}$ and $4d_{5/2}$ states and Yb $5p_{1/2}$ and $5p_{3/2}$ states can be seen at 32.40, 31.30, 26.70, and 23.45 eV respectively. A distinct and sharp doublet structure with a width of ~3 eV dominates the Fermi edge region due mainly to the final state multiplets, $^2F_{5/2}$ and $^2F_{7/2}$, from the photoionization of a $4f$ electron from the filled Yb^{2+} shell. A broad multiplet structure is also visible between 4-13 eV that has been identified as the $4d$-$4f$ resonance enhanced emission from oxidized Yb^{3+}. Figure 4 shows a fit to this region using the energy separations observed for the final state multiplets of oxidized Yb in the $4f^{13}$ configuration.[34-36] The presence of Yb^{3+} was initially thought to indicate mixed valency of Yb, but further detailed study of the Sb3d/O1s region indicates that a small amount of residual oxide contamination remains. The spectrum taken at $h\nu$ = 900 eV in Figure 1 was measured in order to take advantage of the enhanced ionization cross section for O $1s$ at this photon energy, and indicates a small shoulder, nearly coincident with the Sb $3d_{5/2}$, present at 536.5 eV corresponding to residual surface oxide contamination.

The identification of Mn core states is much more difficult than the Yb or Sb states due to Mn occupying less than 4% of the total structure. The low concentration of Mn results in the peak intensities being quite low, and the spin-orbit split states not being well resolved. Despite the low concentration of Mn, the 2*p* core level can be seen in the wide survey at ~648.0 eV, but in order to accurately identify the Mn core and valence band states, a resonant photoemission experiment was performed. With the resonant photoemission experiment, an enhancement of the direct photoemission process occurs due to a second indirect channel opening up as the absorption threshold of a core level is crossed.[37] For this experiment, the indirect transition occurs by initial excitation of a 2*p* electron to an unoccupied 3*d* level forming a bound intermediate state ($2p^6 3d^5$ _ $2p^5 3d^6$), followed by autoionization decay to a final state ($2p^5 3d^6$ _ $2p^6 3d^5 + e^-$) identical to the final state of the direct photoemission process for the ejected electron. Figure 5 shows the "On resonance" and "Off resonance" scans from 0-70 eV binding energy with an inset showing the Mn $2p_{1/2}$ and $2p_{3/2}$ peaks used to identify the photon energy for the resonance scans. The "On resonance" scan was measured with $h\nu$ = 640.6 eV corresponding to the Mn $2p_{3/2}$ peak position, and the "Off resonance" scan was measured with $h\nu$ = 639.0 eV corresponding to an energy below the absorption threshold. From Figure 5, a large difference between the on and off resonance scans can be seen with an onset at 47.2 eV corresponding to the Mn 3*p* core level. There is another enhanced region from 2.7-8.9 eV that can be assigned to the Mn 3*d* and *dp* hybridized states of Mn 3*d* and Sb 5*p*. This assignment arises from comparison to density of states calculations performed on the structural analogs $Ca_{14}MnBi_{11}$ and $Ba_{14}MnBi_{11}$.[29] This study indicates that the majority *d* states lie in a region centered at 2.7 eV below E_F, and that they

hybridize with all states above this region made up mostly of states of *p* character. Accurate identification of the Mn and Sb hybridized states in the valence edge of $Yb_{14}MnSb_{11}$ suffers from the dominance of the Yb^{2+} 4*f* multiplet, but a resonant photoemission scan of the 4*f* region to enhance the Mn states and minimize the Yb states reveals a small contribution of Mn to the valence edge as shown in Figure 6.

Figure 7 shows the wide survey photoemission spectrum of $Yb_{14}ZnSb_{11}$measured at $h\nu$ = 1250 eV. The positions of the core level states for Yb and Sb are present at comparable positions to the Mn analog, and the Zn core levels are also present at their corresponding positions. The Sb 3*s*, $3p_{1/2}$, $3p_{3/2}$, $3d_{3/2}$, $3d_{5/2}$, and 4*s* core levels are observed at binding energies of 948.0, 817.0, 771.0, 542.0, 532.0, and 157.0 eV respectively in addition to the Sb 4*p* core level at 106.0 eV. Similarly, the Yb 4*s*, $4p_{1/2}$, $4p_{3/2}$, $4d_{3/2}$, and $4d_{5/2}$ core levels are present at binding energies of 484.0, 394.0, 345.0, 195.0, and 187.0 eV respectively. In contrast to $Yb_{14}MnSb_{11}$, where the Mn core level *p* states are not well resolved, the Zn spin-orbit split $2p_{1/2}$ and $2p_{3/2}$ core states are clearly observable in the wide survey at 1049.0 and 1027.0 eV respectively. All of these peak positions correspond within <6 eV of the tabulated peak positions for the elemental form, and the peak separations of the spin-orbit split partners correspond to the tabulated differences to within ~1 eV.

Figure 8 shows the valence band scan of $Yb_{14}ZnSb_{11}$ measured at $h\nu$ = 120 eV. In a similar fashion to $Yb_{14}MnSb_{11}$, the general spectral shape of the complete region studied remained consistent over the complete photon energy range studied ($h\nu$ = 80-200 eV). The core level, spin-orbit split Sb $4d_{3/2}$ and $4d_{5/2}$ states and Yb $5p_{1/2}$ and $5p_{3/2}$ states can be seen at 33.60, 32.60, 27.60, and 24.20 eV respectively. A sharp doublet structure

corresponding to the Yb^{2+} 4*f* multiplet is also present at and dominates the Fermi edge region. The final state multiplets of $^2F_{5/2}$ and $^2F_{7/2}$ are slightly broader than the Mn analog and extend over a region of ~ 4 eV. The broad multiplet structure from the Yb^{3+} 4*d*-4*f* resonance enhanced emission between 4-13 eV is also present, but the intensity is much greater than that for the Mn analog and is almost equivalent in magnitude to the Yb^{2+} multiplet. Figure 9 shows the analogous fit of the Yb^{3+} region of $Yb_{14}ZnSb_{11}$ using the same energy separations of the final state multiplets of oxidized Yb^{3+}. Although the presence of Yb^{3+} is enhanced by a similar surface oxidation as seen in the measurements of $Yb_{14}MnSb_{11}$, the mixed valency of Yb is consistent for the Zn analog to the proposal made by Fisher *et al* (Reference 30).

The intermediate Yb valence was also thought to cause the Fermi energy to cross the Yb 4*f* levels more so than the Mn analog. Figure 10 shows a comparison of the Fermi edge for $Yb_{14}MnS_{11}$, $Yb_{14}ZnSb_{11}$, and the Au film used to reference E_F. Both systems have a very low density of states at E_F, and even though both systems are considered metallic conductors (more accurately weakly metallic)[7,12,30], the slow and gradual decrease of the valence edge density of states is more akin to semimetallic behavior as seen in XPS measurements of elemental As, Sb and Bi.[38-40] $Yb_{14}ZnSb_{11}$ shows a slightly higher Yb 4*f* density of states at E_F indicating slightly more metallic behavior, and also is in agreement with the proposal of a shift of the Yb 4*f* levels across E_F due to a mixed Yb valency.

In conclusion, the measurements of core and valence electronic states of single crystals of the rare earth transition metal Zintl phases $Yb_{14}MnSb_{11}$ and $Yb_{14}ZnSb_{11}$ are presented in addition to the crystal structure of $Yb_{14}ZnSb_{11}$. The crystal structure is

similar to that reported for $Yb_{14}MnSb_{11}$ with the site occupancy factors indicating full occupancies (within the range of their standard deviations) in all sites except the Zn site. Sample surfaces of $Yb_{14}MnSb11$ and $Yb14ZnSb_{11}$ were measured as received, after Ar^+ ion bombardment, and after cleaving *in situ*. Detailed analysis of the clean Mn and Zn analog sample surfaces reveal a significant contribution of both Yb^{3+} and Yb^{2+} 4*f* states in the valence band region for the Zn analog and no contribution of Yb^{3+} states to the valence band for the Mn analog. This result is predicted for the Zn analog as an intermediate Yb valence by Zintl counting rules and thermodynamic, transport, and single crystal X-ray diffraction studies. A slightly higher density of states at E_F for $Yb_{14}ZnSb_{11}$ compared to $Yb_{14}MnSb_{11}$ is also observed, and is consistent with the proposal of a shift of the Yb 4*f* states across E_F due to an intermediate Yb valence.

Acknowledgements.

We thank R.N. Shelton for use of the magnetometer and P. Klavins for technical assistance. We also thank the staff of the Advanced Light Source and Beamline 4.0 for their assistance. This research is funded by the National Science Foundation DMR-9803074, 0120990, by the Materials Research Institute through LLNL, by Campus Laboratory Collaborations Program of the University of California, and was performed under the auspices of the U.S Department of Energy by Lawrence Livermore National Laboratory under contract no. W-7405-Eng-48.

References.

(1) Cordier, G.; Schäfer, H.; Stelter, M. *Zeitschrift fur Anorganische und Allgemeine Chemie* **1984**, *519*, 183-188.

(2) Kauzlarich, S. M. In *Chemistry, Structure, and Bonding of Zintl Phases and Ions*; Kauzlarich, S. M., Ed.; VCH Publishers, Inc.: New York, 1996, pp 245-274.

(3) Kauzlarich, S. M.; Payne, A. C.; Webb, D. J. In *Magnetism: Molecules to Materials III*; Miler, J. S., Drillon, M., Eds.; Wiley-VCH: Weinham, 2002, pp 37-62.

(4) Kauzlarich, S. M., Ed. *Chemistry, Structure, and Bonding of Zintl Phases and Ions*; VCH Publishers, Inc.: New York, 1996.

(5) Brock, S. L.; Weston, L. J.; Olmstead, M. M.; Kauzlarich, S. M. *J Solid State Chem* **1993**, *107*, 513-523.

(6) Chan, J. Y.; Kauzlarich, S. M.; Klavins, P.; Shelton, R. N.; Webb, D. J. *Chem Mater* **1997**, *9*, 3132-3135.

(7) Chan, J. Y.; Olmstead, M. M.; Kauzlarich, S. M.; Webb, D. J. *Chem Mater* **1997**, *10*, 3583 - 3588.

(8) Chan, J. Y.; Wang, M. E.; Rehr, A.; Kauzlarich, S. M.; Webb, D. J. *Chemistry of Materials*. **1997**, *9*, 2131 - 2138.

(9) Chan, J. Y.; Kauzlarich, S. M.; Klavins, P.; Shelton, R. N.; Webb, D. J. *Phys Rev B* **1998**, *57*, 8103 - 8106.

(10) Chan, J. Y.; Kauzlarich, S. M.; Klavins, P.; Liu, J.-Z.; Shelton, R. N.; Webb, D. J. *Phys Rev B* **2000**, *61*, 459-463.

(11) Del Castillo, J.; Webb, D. J.; Kauzlarich, S. M.; Kuromoto, T. Y. *Phys Rev B* **1993**, *47*, 4849-4852.

(12) Fisher, I. R.; Wiener, T. A.; Bud'ko, S. L.; Canfield, P. C.; Chan, J. Y.; Kauzlarich, S. M. *Phys Rev B* **1999**, *59*, 13829-13834.

(13) Gallup, R. F.; Fong, C. Y.; Kauzlarich, S. M. *Inorganic Chemistry* **1992**, *31*, 115-118.

(14) Kauzlarich, S. M.; Kuromoto, T. Y.; Olmstead, M. M. *J Am Chem Soc* **1989**, *111*, 8041-8042.

(15) Kauzlarich, S. M.; Kuromoto, T. Y. *Croatica Chemica Acta* **1991**, *64*, 343-352.

(16) Kauzlarich, S. M.; Thomas, M. M.; Odink, D. A.; Olmstead, M. M. *J Am Chem Soc* **1991**, *113*, 7205-7208.

(17) Kuromoto, T. Y.; Kauzlarich, S. M.; Webb, D. J. *Molecular Crystals and Liquid Crystals* **1989**, *181*, 349-357.

(18) Kuromoto, T. Y.; Kauzlarich, S. M.; Webb, D. J. *Chem Mater* **1992**, *4*, 435-440.

(19) Payne, A. C.; Olmstead, M. M.; Kauzlarich, S. M.; Webb, D. J. *Chem Mater* **2001**, *13*, 1398-1406.

(20) Rehr, A.; Kauzlarich, S. M. *Journal of Alloys and Compounds* **1994**, *207*, 424-426.

(21) Rehr, A.; Kuromoto, T. Y.; Kauzlarich, S. M.; Del Castillo, J.; Webb, D. J. *Chem Mater* **1994**, *6*, 93-99.

(22) Siemens, D. P.; Del Castillo, J.; Potter, W.; Webb, D. J.; Kuromoto, T. Y.; Kauzlarich, S. M. *Solid State Communications* **1992**, *84*, 1029-1031.

(23) Webb, D. J.; Kuromoto, T. Y.; Kauzlarich, S. M. *Journal of Magnetism and Magnetic Materialsm* **1991**, *98*, 71-75.

(24) Webb, D. J.; Kuromoto, T. Y.; Kauzlarich, S. M. *Journal of Applied Physics* **1991**, *69*, 4825.

(25) Webb, D. J.; Cohen, R.; Klavins, P.; Shelton, R. N.; Chan, J. Y.; Kauzlarich, S. m. *Journal of Applied Physics* **1998**, *83*, 7192-7194.

(26) Young, D. M.; Torardi, C. C.; Olmstead, M. M.; Kauzlarich, S. M. *Chem Mater* **1995**, *7*, 93-101.

(27) Holm, A. P.; Kauzlarich, S. M.; Morton, S. A.; Waddill, G. D.; Pickett, W. E.; Tobin, J. G. *J Am Chem Soc* **2002**, *124*, 9894-9898.

(28) Kim, H.; Chan, J. Y.; Olmstead, M. M.; Klavins, P.; Webb, D. J.; Kauzlarich, S. M. *Chem Mater* **2002**, *14*, 206-216.

(29) Sánchez-Portal, D.; Martin, R. M.; Kauzlarich, S. M.; Pickett, W. E. *Phys Rev B* **2002**, *65*, 144414(144411-144415).

(30) Fisher, I. R.; Bud'ko, S. L.; Song, C.; Canfield, P. C.; Ozawa, T. C.; Kauzlarich, S. M. *Physical Review Letters* **2000**, *85*, 1120-1123.

(31) Canfield, P. C.; Fisk, Z. *Philosophical Magazine B* **1992**, *65*, 1117-1123.

(32) Sheldrick, G. M.; 5.10 ed.; Bruker AXS Inc.: Madison, Wisconsin, 1997.

(33) Cardona, M.; Ley, L. *Topics in Applied Physics* **1978**, *26*.

(34) Suga, S.; Ogawa, S.; Namatame, H.; Taniguchi, M.; Kakizaki, A.; Ishii, T.; Fujimori, A.; Oh, S.-J.; Kato, H.; Miyahara, T.; Ochiai, A.; Suzuki, T.; Kasuya, T. *Journal of the Physical Society of Japan* **1989**, *58*, 4534-4543.

(35) Mori, T.; Soda, K.; Yamamoto, M.; Namatame, H.; Ochiai, A.; Suzuki, T.; Kasuya, T.; Suga, S. *Journal of the Physical Society of Japan* **1987**, *56*, 1465-1469.

(36) Johansson, L. I.; Allen, J. W.; Lindau, I.; Hecht, M. H.; Hagström, S. B. M. *Phys Rev B* **1980**, *21*, 1408-1411.

(37) Mishra, S. R.; Cummins, T. R.; Waddill, G. D.; Gammon, W. J.; van der Laan, G.; Goodman, K. W.; Tobin, J. G. *Physical Review Letters* **1998**, *81*, 1306-1309.

(38) Jezequel, G.; Petroff, Y.; Pinchaux, R.; Yndurain, F. *Phys Rev B* **1986**, *33*, 4352-4355.

(39) Jezequel, G.; Thomas, J.; Pollini, I. *Phys Rev B* **1997**, *56*, 6620-6626.

(40) Tokailin, H.; Takahashi, T.; Sagawa, T.; Shindo, K. *Phys Rev B* **1984**, *30*, 1765-1772.

Table 1. Data collection parameters and crystallographic data for $Yb_{14}ZnSb_{11}$.

Empirical formula	$Yb_{14}ZnSb_{11}$
Crystal size (mm)	0.03 × 0.178 × 0.142
Space group	$I4_1/acd$
Z	8
Temperature (K)	90
Unit cell dimensions (Å)	a = 16.562(3)
	c = 21.859(2)
Volume (Å^3)	5995.9(16)
Formula weight (g/mol)	3827.18
Reflections collected	27196
Unique reflections	2493
Parameters refined	63
Max. and min. transmission	0.4134 and 0.0330
μ Mo Kα (mm^{-1})	26.83
R1 [I>2σ(I)][a]	0.0438
wR2[b]	0.0841

[a] $R1 = ||F_0|-|F_c||/\Sigma|F_0|$

[b] $wR2 = \sqrt{[\Sigma[w(F_0^2-F_c^2)^2]/\Sigma[w(F_0^2)^2]}$

Table 2. Atomic coordinates, site occupancy, and anisotropic displacement parameters ($Å^2$).

site	x	y	z	SOF	U_{eq} [a]
Sb(1)	0.13556(4)	0.38556(4)	0.125	1	0.00403(18)
Sb(2)	0.00440(4)	0.10934(4)	0.81037(3)	1	0.00457(15)
Sb(3)	0.86954(4)	0.97338(4)	0.95268(3)	1	0.00497(15)
Sb(4)	0.0000	0.2500	0.1250	1	0.0048(3)
Yb(1)	-0.04223(3)	-0.07373(3)	0.828290(17)	1	0.00458(11)
Yb(2)	-0.02164(3)	0.12496(3)	0.001630(18)	1	0.00601(11)
Yb(3)	0.35534(4)	0.0000	0.2500	1	0.00425(13)
Yb(4)	0.17998(3)	0.40937(3)	0.842610(18)	1	0.00601(11)
Zn(1)	0.0000	0.2500	0.8750	0.976(11)	0.0053(7)

[a] Ueq is defined as one-third of the trace of the orthogonalized U_{ij} tensor.

Table 3. Selected inter-atomic distances (Å) and angles (°).

Sb(1)-Sb(4)	3.1750(11)
Sb(1)-Yb(1) × 2	3.1750(11)
Sb(1)-Yb(2) × 2	3.2958(7)
Sb(1)-Yb(3)	3.3288(5)
Sb(1)-Yb(4)	3.1607(10)
Sb(2)-Zn × 4	2.7255(8)
Sb(2)-Yb(1)	3.1531(10)
Sb(2)-Yb(1')	3.1830(8)
Sb(2)-Yb(2)	3.6957(10)
Sb(2)-Yb(2')	3.1169(9)
Sb(2)-Yb(3)	3.2276(10)
Sb(2)-Yb(4)	3.1492(10)
Sb(2)-Yb(4')	3.3925(9)
Sb(3)-Yb(1)	3.1680(10)
Sb(3)-Yb(1')	3.1840(8)
Sb(3)-Yb(2)	3.1617(10)
Sb(3)-Yb(2')	3.2704(10)
Sb(3)-Yb(3)	3.1250(10)
Sb(3)-Yb(4)	3.1989(8)
Sb(3)-Yb(4')	3.1782(8)
Sb(3)-Yb(4")	3.6896(11)
Sb(4)-Yb(1) × 4	3.1709(7)
Sb(4)-Yb(2) × 4	3.4190(5)
Sb(2)-Zn-Sb(2')	105.584(14)
Sb(2)-Zn-Sb(2")	117.56(3)
Zn□ Zn	9.9216(13)

Figure Captions.

Figure 1. A comparison of scans of the Sb3d/O1s region (520-540 eV) of the "as-received", Ar^+ sputtered, and cleaved sample surfaces.

Figure 2. The wide survey photoemission spectrum of $Yb_{14}MnSb_{11}$ measured at $h\nu$ = 1250 eV. Scans of the "as-received" samples show slight Sn contamination, but upon cleaving, all indications of Sn are removed as seen in the inset.

Figure 3. The valence band scan of $Yb_{14}MnSb_{11}$ measured at $h\nu$ = 120 eV.

Figure 4. Gaussian function fit to the Yb^{3+} 4*f* region of $Yb_{14}MnSb_{11}$ using the energy separations observed for the final state multiplets of oxidized Yb in the $4f^{13}$ configuration

Figure 5. The "On resonance" and "Off resonance" scans from 0-70 eV binding energy with an inset showing the Mn $2p_{1/2}$ and $2p_{3/2}$ peaks used to identify the photon energy for the resonance scans of $Yb_{14}MnSb_{11}$.

Figure 6. Resonant photoemission scan of the 4*f* region of $Yb_{14}MnSb_{11}$.

Figure 7. The wide survey photoemission spectrum of $Yb_{14}ZnSb_{11}$ measured at $h\nu$ = 1250 eV.

Figure 8. The valence band scan of $Yb_{14}ZnSb_{11}$ measured at $h\nu$ = 120 eV.

Figure 9. Gaussian fit of the Yb^{3+} region of $Yb_{14}ZnSb_{11}$ using the same energy separations of the final state multiplets as used for the $Yb_{14}MnSb_{11}$ scan.

Figure 10. Comparison of the Fermi edge for $Yb_{14}MnS_{11}$, $Yb_{14}ZnSb_{11}$, and the Au film used to reference E_F.

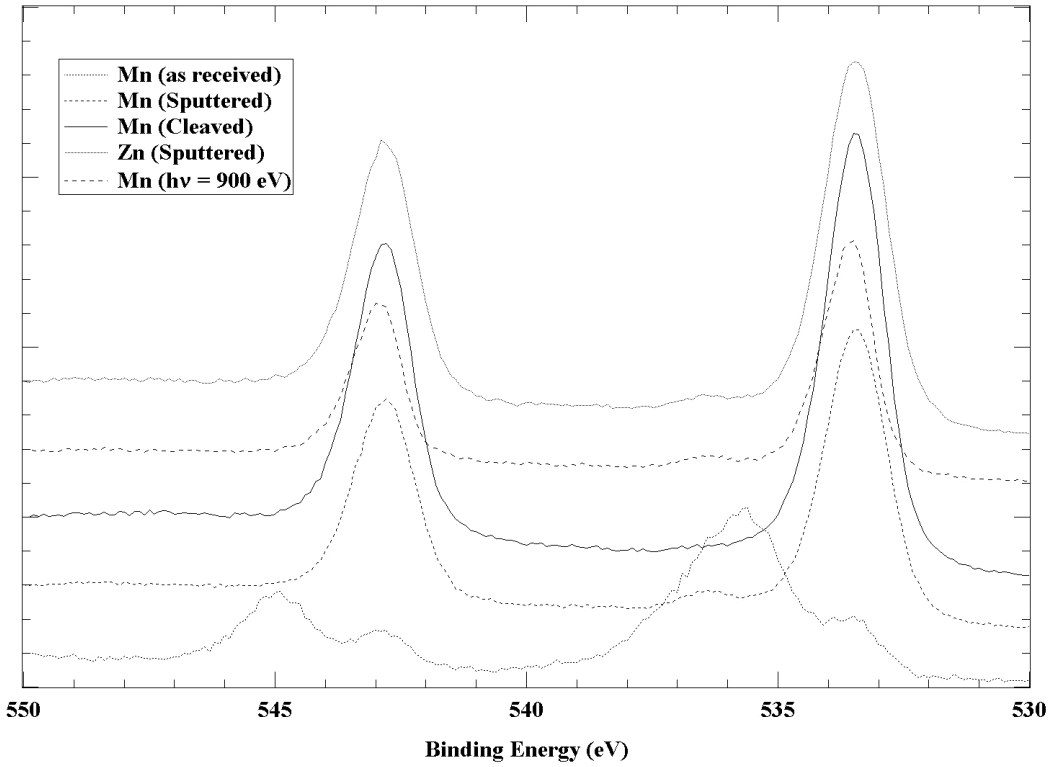
Mn (as received)
Mn (Sputtered)
Mn (Cleaved)
Zn (Sputtered)
Mn (hν = 900 eV)
550
545
540
535
530
Binding Energy (eV)

Figure 1.

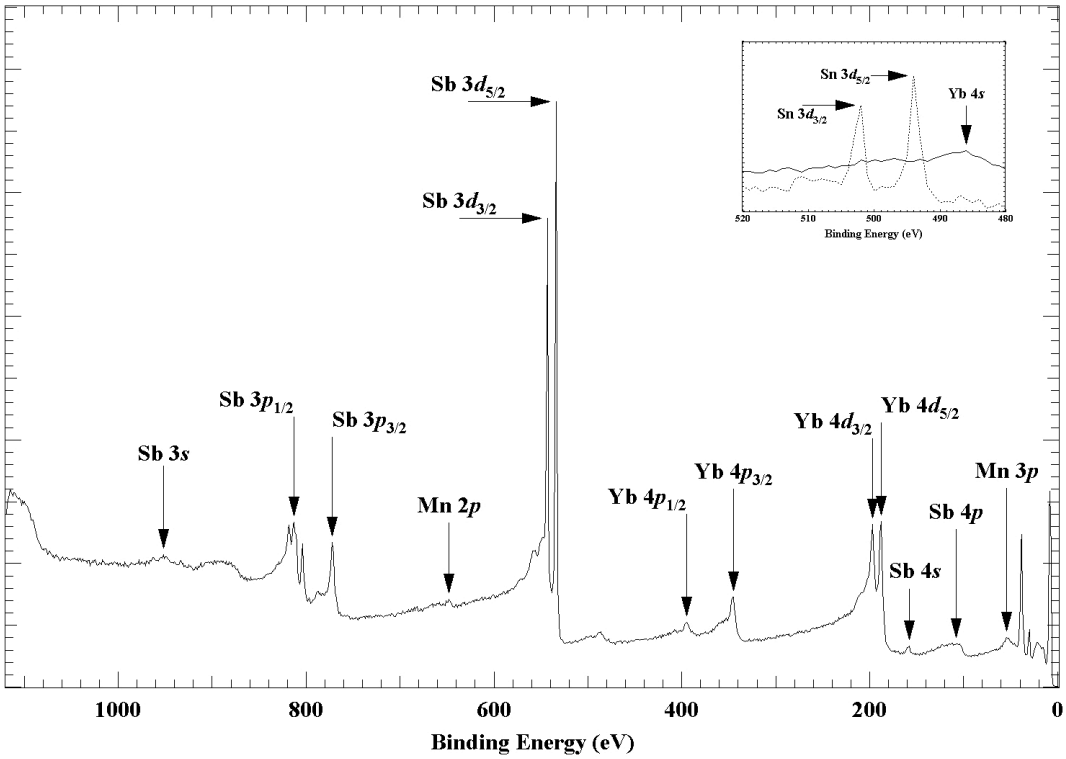

Figure 2. $Yb_{14}MnSb_{11}$.

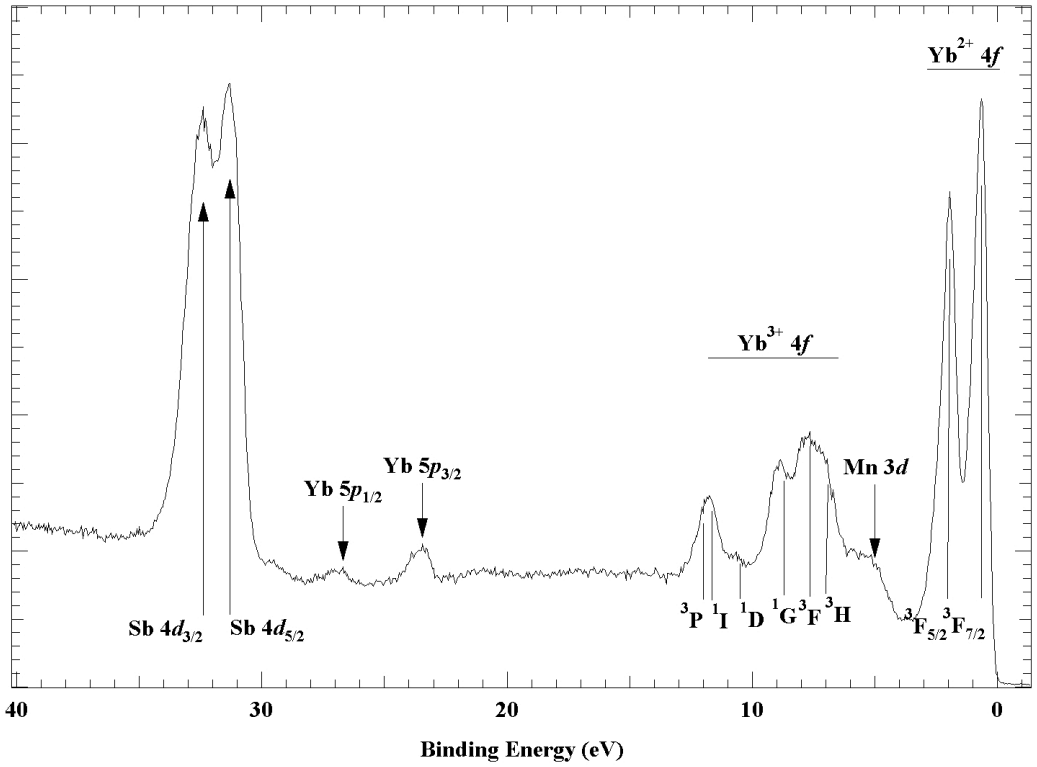

Figure 3. $Yb_{14}MnSb_{11}$

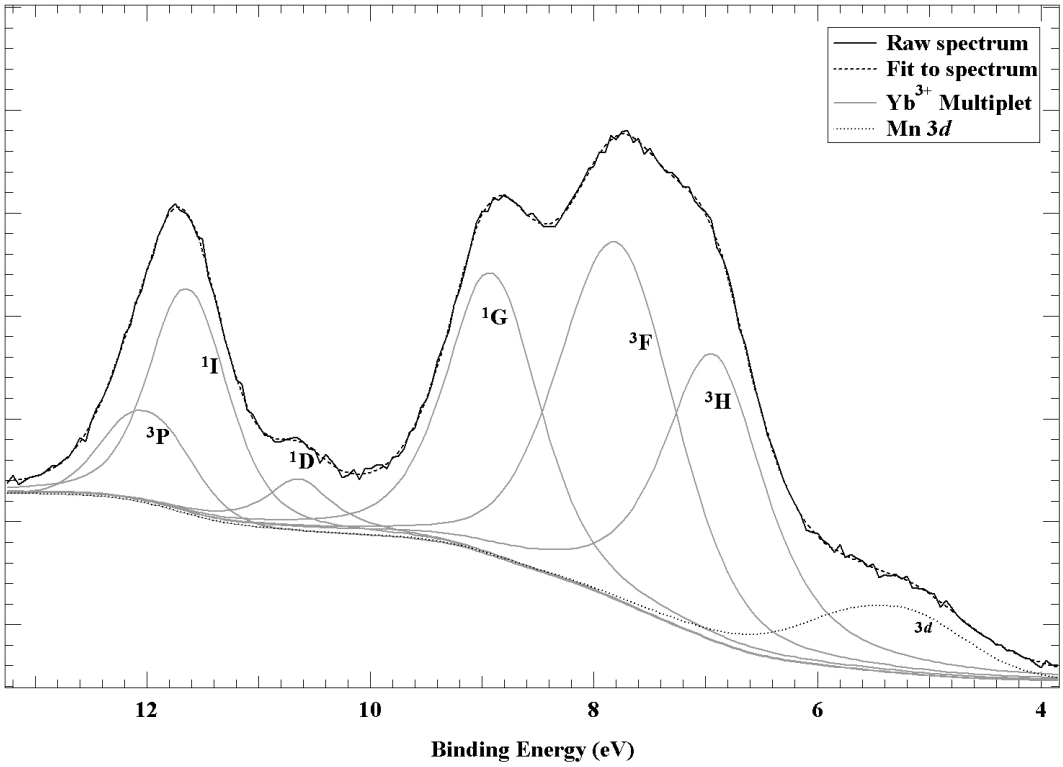

Figure 4. $Yb_{14}MnSb_{11}$

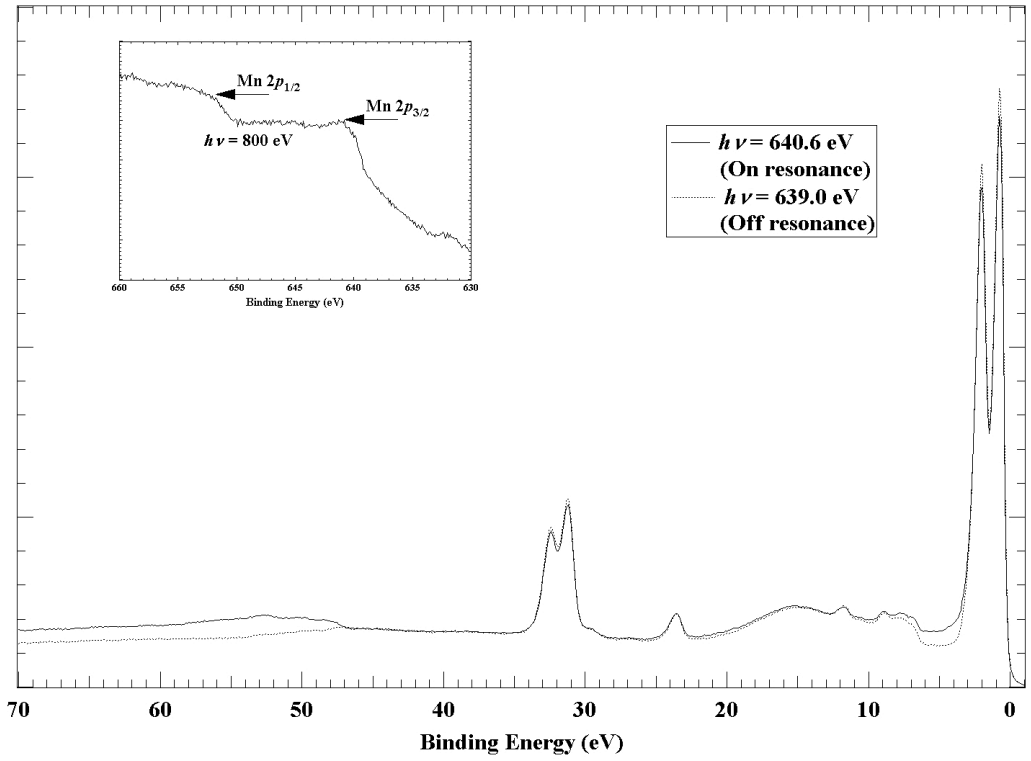

Figure 5. $Yb_{14}MnSb_{11}$.

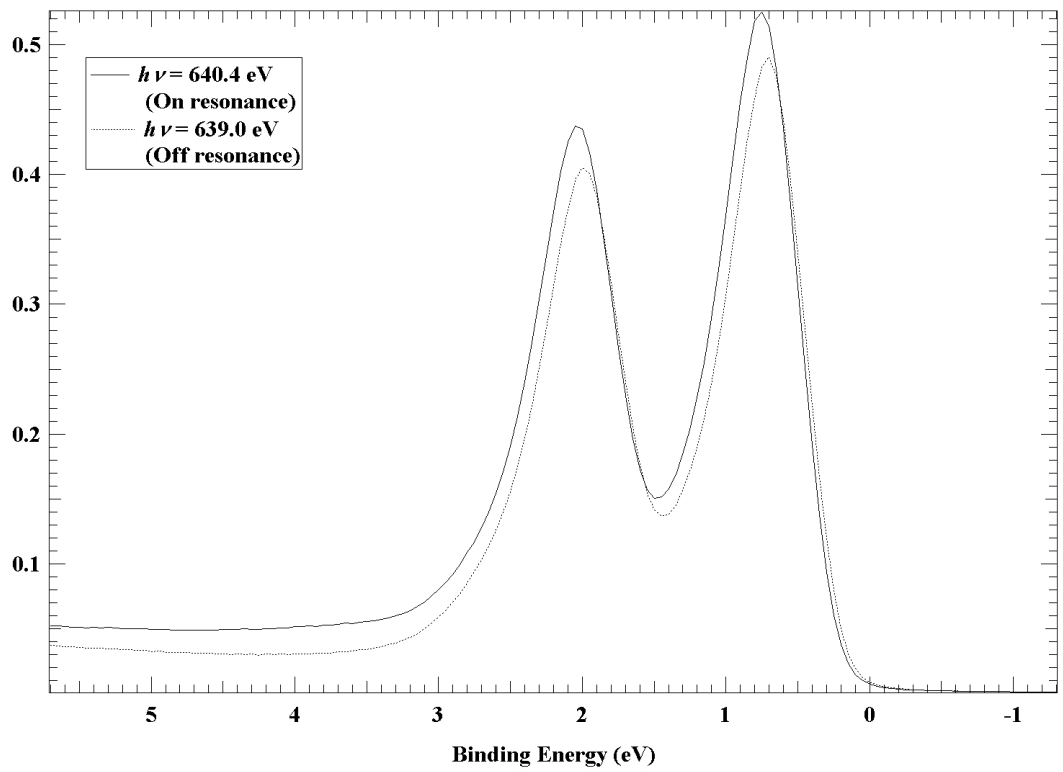

Figure 6. $Yb_{14}MnSb_{11}$

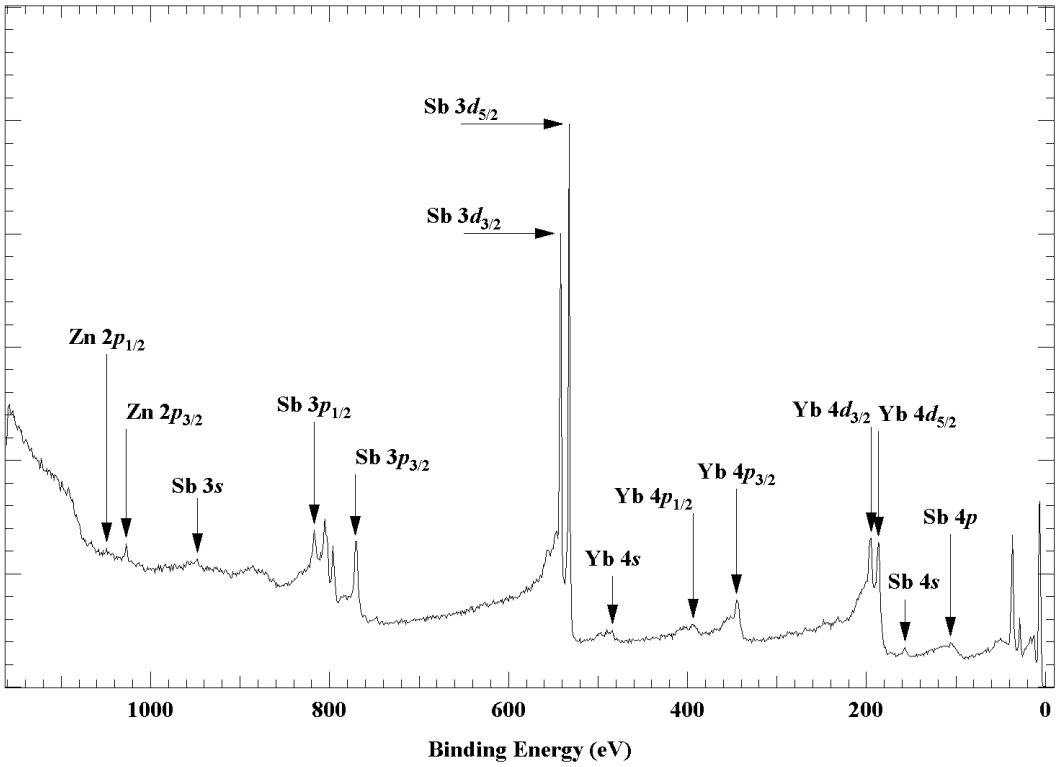

Figure 7. $Yb_{14}ZnSb_{11}$

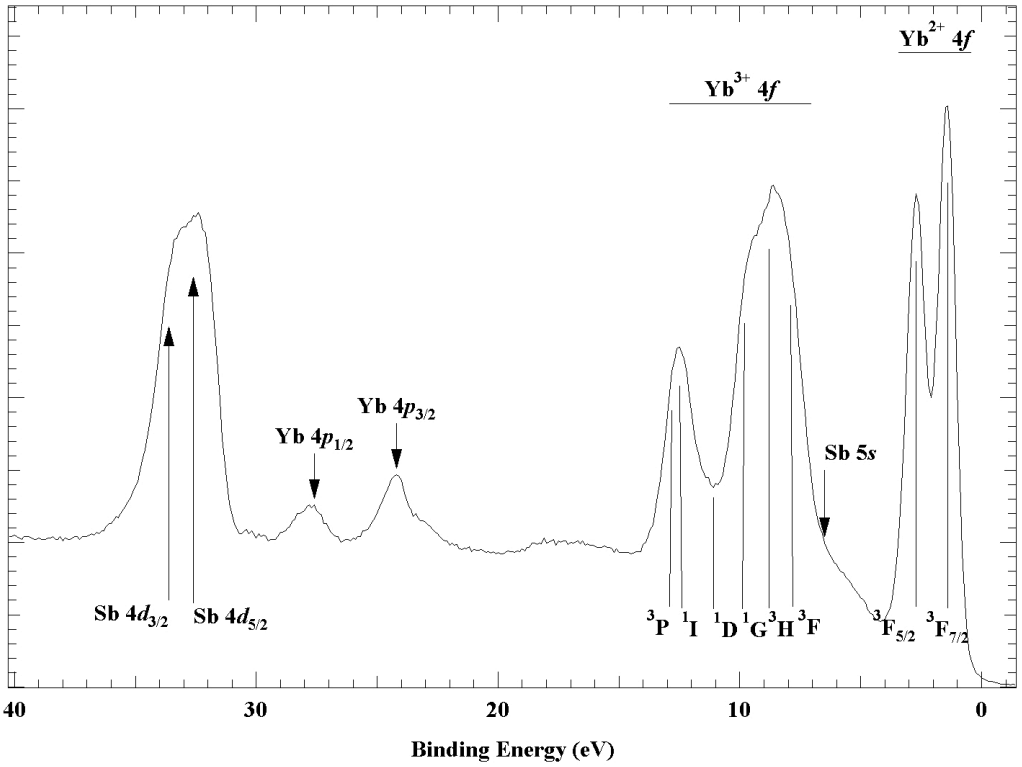

Figure 8. $Yb_{14}ZnSb_{11}$.

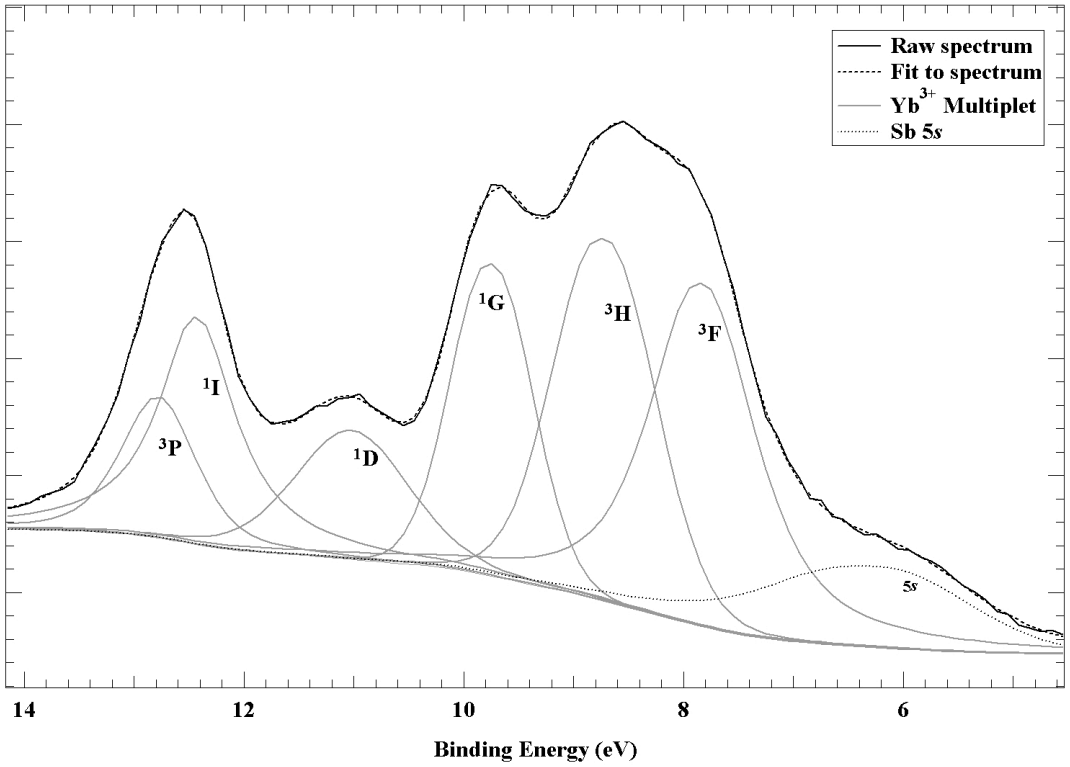

Figure 9. $Yb_{14}ZnSb_{11}$

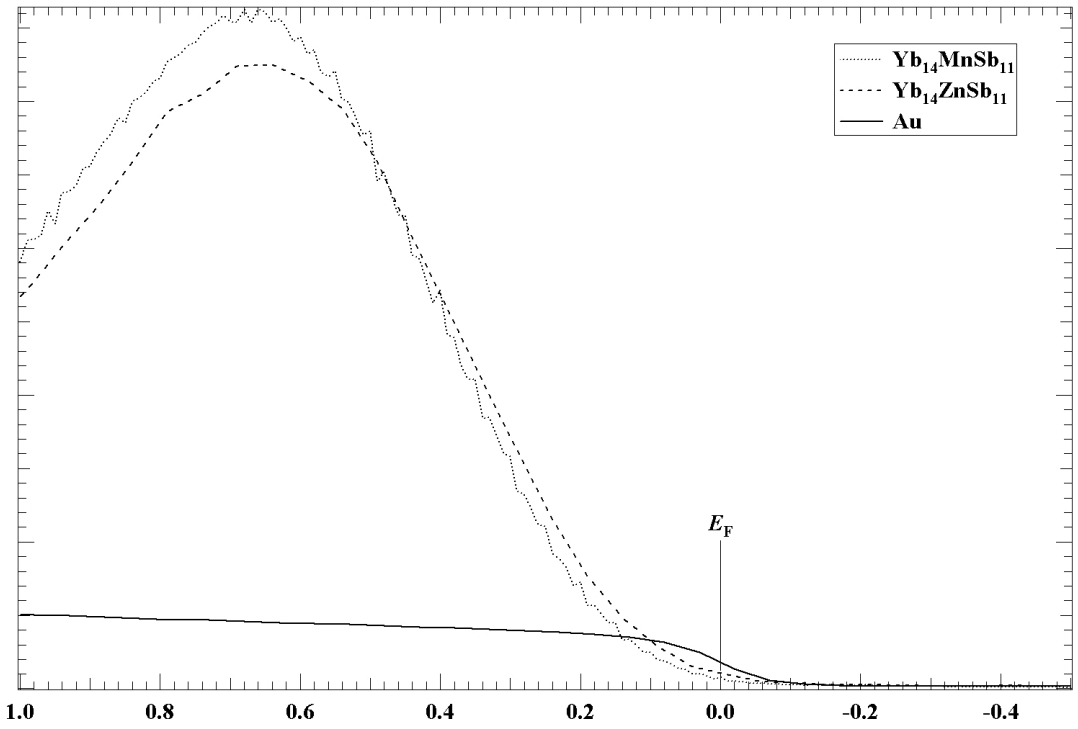

Figure 10.